

# Modeling of quantum-coherence effects in heavy-ion induced parton energy loss

Weiyao Ke, Yingru Xu, and Steffen A. Bass

*Department of Physics, Duke University, Durham, NC 27708-0305*

(Dated: September 23, 2018)

Modeling of the space-time evolution of highly energetic partons created in perturbative processes at the onset of relativistic heavy-ion collisions has become a valuable tool for the study of hot and dense deconfined QCD matter. This is accomplished by relating the energy-loss of these partons to the properties of the medium they traverse. Monte-Carlo event generators, that allow for the realistic description of fluctuating initial conditions and medium properties, have become a powerful tool in this endeavor. However, the implementation of quantum coherence effects, such as the Landau-Pomeranchuk-Migdal (LPM) effect, poses a serious challenge to this class of models, since multiple parton interactions cannot be factorized into independent processes. In this work, we discuss several common implementations of the LPM effect in Monte-Carlo event generators and compare them to limiting cases in jet energy-loss theory for which semi-analytic calculations exist. We propose an approach, dubbed “modified rescattering”, that reproduces the limiting semi-analytic calculations of radiative parton energy loss for infinite and thin media and reasonably describes gluon emission spectra in a static medium. We study the impact of an expanding medium, a running coupling and heavy quark masses in this approach.

## I. INTRODUCTION

The study of hard probes in relativistic heavy-ion collisions is moving towards the precision era thanks to upcoming experimental upgrades [1–5] as well as theoretical and computational advances that allow for the execution of jet energy-loss calculations in a realistic Quark-Gluon-Plasma (QGP) medium (including event-by-event fluctuating initial conditions and temperature-dependent transport coefficients). Among the goals for this research is the characterization of the QGP medium in terms of its jet energy-loss transport coefficients.

Monte-Carlo event generators that allow for the realistic description of fluctuating initial conditions and medium properties, have become a powerful tool in this endeavor. However, the implementation of quantum coherence effects, such as the Landau-Pomeranchuk-Migdal (LPM) effect, poses a serious challenge to this class of models, since multiple parton interactions cannot be factorized into independent processes. In a dense medium, the LPM effect is important for the treatment of radiative energy-loss, which is the dominant contribution to energy-loss of partons traversing the QGP at high momentum. Here, multiple scatterings during the gluon formation time act coherently to suppress the radiation spectrum [6–9]. Therefore, a medium induced radiation becomes effectively an  $n$ -body to  $(n+1)$ -body process that extends in space-time. This feature is particularly difficult to be accurately implemented in a Monte-Carlo way, where interactions are usually based on few-body processes that are local. To simplify the problem while still keep the essential qualitative features such as the characteristic emission spectrum and path-length dependent energy loss, different methods have been used in numerical simulations [10–16]. In this work we compare three of the most common implementations based on different approximations of radiative energy-loss in idealized limits. As we shall see, a modified approach based the

method of [14] works remarkably well. This method, referred to as the “Modified rescattering” approach, reproduces analytic calculations of energy loss as a function of coupling constant, temperature, parton energy and path lengths. It also reasonably well describes the gluon radiation spectrum. We introduce parameters to control its finite- and infinite-size behaviors separately. The parameters can be fine-tuned to match the theory or be calibrated to experimental data; therefore, the performance of the theory can be measured quantitatively on the landscape of this parameter space in future statistical analysis.

This paper is organized as follows. Section II reviews the qualitative spectrum of the medium induced radiation. In Section III, three Monte Carlo implementations of the radiative processes are discussed. Semi-analytic results to which the Monte Carlo simulations are compared are briefly summarized in Section IV. The major results are discussed in Section V. Finally, we discuss in Section VI the running coupling effect, expanding medium effect and the mass (dead-cone) effect in the “Modified rescattering” implementation. We summarize in Section VII.

## II. QUALITATIVE FEATURES OF THE MEDIUM INDUCED RADIATION

In this section, we introduce the qualitative features of the medium induced radiation following the discussion in [9]. A radiated gluon stays in coherence with the mother partons for a finite amount of time determined by the uncertainty principle  $\Delta t \sim 1/\Delta E$ .  $\Delta E$  is the difference in light-cone energy between the initial mother parton energy  $E$  and the final state of daughter partons. The formation time is then,

$$\tau_f \sim \frac{2(1-x)\omega}{k_\perp^2 + (1-x)m_g^2}. \quad (1)$$

$x = \omega/E$  is the energy fraction carried by the gluon.  $m_g^2$  is the gluon thermal mass squared is related to the Debye screening mass by  $m_g^2 = m_D^2/2 \sim \alpha_s T^2$ . For a collinear splitting, the formation time looks like  $\omega/(\alpha_s T^2)$ . Meanwhile, the gluon can keep interacting with the dense medium via elastic collisions with a rate  $R_g$  that scales like  $\alpha_s T$ . Therefore, the number of rescatterings within the formation time  $N \sim \tau_f R_g \sim \omega/T$  may not be a small number for gluon with energy comparable or larger than the medium temperature. Because rescatterings also change the transverse momentum  $k_\perp$  of the gluon relative to the mother parton, a self-consistent formation time estimation is required. Given that on average elastic scattering increases  $k_\perp^2$  by an amount  $\hat{q}_g \tau_f$  where  $\hat{q}_g = d\langle k_\perp^2 \rangle/dt$  is the gluon transport coefficient, the self-consistent relation for an averaged formation time is,

$$\tau_f \sim \frac{2(1-x)\omega}{\hat{q}_g \tau_f} \longrightarrow \tau_f \sim \sqrt{\frac{2(1-x)\omega}{\hat{q}_g}} \quad (2)$$

The inverse of the formation time measures the rate of a gluon being separated from the mother parton.

The radiation spectrum is understood as follows. A virtual gluon with energy  $\omega$  and transverse momentum  $k_\perp$  splits from the mother parton with the probability given by the vacuum splitting function ( $P(x) \sim \alpha_s/x$ ). If its formation time is smaller than the mean-free-path of elastic scattering  $\lambda_g = 1/R_g$ , it is put on shell with the rate  $1/\lambda_g$  (the Bethe-Heitler region); otherwise multiple rescatterings put it on-shell with a rate  $1/\tau_f$  (the LPM region). As a result, the differential radiation rate is,

$$\frac{dP}{dt d\omega} \sim \begin{cases} \frac{\alpha_s}{\omega} \frac{1}{\lambda_g} \sim \alpha_s^2 \frac{T}{\omega}, & \tau_f \lesssim \lambda_g \\ \frac{\alpha_s}{\omega} \frac{1}{\tau_f} \sim \alpha_s \sqrt{\hat{q}_g/T^3} \left(\frac{T}{\omega}\right)^{3/2}, & \lambda_g \lesssim \tau_f \end{cases} \quad (3)$$

We note first that in the leading order picture, the LPM effect modifies the single gluon emission rate. It does not introduce correlations between subsequent emissions which are higher order effects [17]. Second, the emission rate at a certain time receives coherent contributions from the collision centers whose locations extend about  $\tau_f$  along the path of the mother parton. Therefore, if the number of scattering centers in a thin medium of size  $\lambda_g < L < \tau_{f,\max} \sim \sqrt{E/\hat{q}_g}$  are limited, the second line of Equation 3 is replaced by,

$$\frac{dP}{dt d\omega} \sim \frac{\alpha_s}{\omega} \frac{1}{\min\{\tau_f, L\}}, \lambda_g < \tau_f \quad (4)$$

The radiative energy loss is obtained by integrating over the differential rate times the gluon energy. For the case of an infinite medium, this is

$$\Delta E / \Delta L \sim \alpha_s^2 \sqrt{ET^3} \quad (5)$$

Therefore for high energy patrons, the amount of energy loss is significantly reduced compared to the incoherent calculation  $\Delta E / \Delta L \sim \alpha_s^2 ET$ . For a thin medium, the

LPM effect leads to the non-linear path length  $L$  dependence of the energy loss

$$\Delta E \sim \alpha_s \hat{q} L^2 \quad (6)$$

When the path length exceeds the  $\tau_{f,\max}$ ,  $\Delta E$  should smoothly transit to the behavior given by Equation 5.

### III. DIFFERENT MONTE-CARLO IMPLEMENTATIONS

Despite there have been many practices of implementing the LPM physics, we compared only those approaches that treat this effect non-locally thus result in a path length dependent spectrum. The framework we worked in is the **Lido** model [18]. It is originally designed for heavy quark transport inside a QGP. In this section, we turn off all quark mass effects (phase-space, matrix-elements) to study light quark first. The **Lido** model is based on elementary ( $2 \rightarrow 2$ ) elastic and inelastic pQCD scatterings. The inelastic processes include both gluon radiation ( $2 \rightarrow 3$ ) and gluon absorption ( $3 \rightarrow 2$ ) processes using an improved Gunion-Bertsch approximated matrix-element [19, 20]. For the comparison to theory calculations, we only turn on the  $2 \rightarrow 3$  channel for the high energy quark and the  $t$ -channel in the elastic scatterings. Next, we introduce three different LPM effect implementations in detail.

*“Coherence factor” approach* This first approach is the old one used in the **Lido** model. It is similar to the higher-twist formula used in the radiation improved Langevin equation [11] and the Linearized-Boltzmann-Transport-Model [21, 22]. In the **Lido** model, we start from the incoherent rate of a  $2 \rightarrow 3$  process using Gunion-Bertsch cross-section  $\sigma_{GB}$ ,

$$\Gamma = \frac{1}{2E_1} \int \frac{f_i(p_2) d\vec{p}_2^3}{(2\pi)^3 2p_2} 2\hat{s} \int d\hat{t} \frac{d\vec{k}^3}{(2\pi)^3 2k} \frac{d\sigma_{GB}}{d\hat{t} d\vec{k}^3} \quad (7)$$

The “Coherence factor” approach implements LPM suppression by multiplying a time-dependent coherence factor to the final state gluon phase space integration in Equation 7,

$$\frac{d\vec{k}^3}{(2\pi)^3 2k} \rightarrow \frac{d\vec{k}^3}{(2\pi)^3 2k} 2 \left[ 1 - \cos \left( \frac{t - t_0}{\tau_f} \right) \right] \quad (8)$$

The modified rate depends on the time separation  $\Delta t = t - t_0$  which is the time elapse from the last gluon emission. If one makes a small angle scattering approximation to the Gunion-Bertsch matrix-element (please refer to Appendix B for details), the Gunion-Bertsch rate can be rewritten into a diffusion induced radiation rate

$$\Gamma = \hat{q}_g \int \frac{\alpha_s}{2\pi} \frac{2C_F dx}{x} \frac{dk_\perp^2}{k_\perp^4}. \quad (9)$$

This would be the same as the one used in [11] if the coherence factor is included. Either way, the value of  $\Delta t$

is only determined at run-time, but we can still estimate its order-of-magnitude from the following condition:

$$\begin{aligned} 1 &\sim \int_0^{\Delta t} \Gamma(t) dt, \\ &= \Delta t \int d\Gamma \left[ 1 - \frac{\sin(\Delta t/\tau_f)}{\Delta t/\tau_f} \right] \end{aligned} \quad (10)$$

which means that the probability to have one radiation within  $\Delta t$  should be of order 1 required by the definition of  $\Delta t$ . A dimensional analysis (Appendix B) shows  $\Delta t \sim 1/\alpha_s T$ . We see that this prescription indeed suppresses the spectrum when the formation time is much greater than the mean-free-path. However, multiple scatterings are not included since gluons are always produced in  $2 \rightarrow 3$  processes. Moreover, it introduces correlation between the locations of vertices of subsequent emissions; especially, no matter how soft the previous radiation is, it affects the next radiation in the same way and the prediction depends on the minimum gluon energy cut-off in a logarithmic way.

The next two approaches both include multiple-scattering in the formation time determination with the method motivated by [14]. A gluon is first sampled from a  $2 \rightarrow 3$  inelastic scattering at time  $t = t_0$ , but it is not immediately regarded as “formed”. This gluon may keep interacting with the medium via elastic processes. Both change the gluon transverse momentum  $k_{\perp,n}$  and formation time  $\tau_{f,n}$  will be changed after each rescattering. Here, the subscripts  $n$  denote the quantities calculated after the  $n$ -th rescattering. This continues until the time elapse since  $t_0$  just exceeds the gluon formation time after the  $n$ -th rescattering,

$$\tau_{f,n} < t - t_0 < \tau_{f,n-1}. \quad (11)$$

After this amount of time, the gluon is considered to have lost coherence with the mother parton. The formation time determined in this way fulfills the self-consistent condition of Equation 2, but it is still tricky to introduce the correct suppression, so we compared the following two approaches.

*“Block radiation” approach* An attempt to introduce suppression is by requiring that no other radiation is allowed within  $t - t_0$  showed in Equation 11, referred to as the “Block radiation” approach in this paper. It certainly suppresses the radiation rate and also results in a non-linear path length dependence of the energy loss; however, a closer examination reveals its problems. First of all, it again introduces correlations between subsequent emission vertices. But the biggest problem is that it does not alter the spectrum shape, because though each branching is delayed by  $\tau_f$ , it is still generated according to the incoherent differential probability. The  $2 \rightarrow 3$  spectrum is only suppressed by an overall factor  $1/N$  that reduces  $N$  possible inelastic collisions to a single one,

$$N \sim \frac{\langle \tau_{f,N} \rangle}{\lambda_{\text{inel}}}. \quad (12)$$

This is also different from the expected qualitative behavior: it is  $\lambda_{\text{el}}$  instead of  $\lambda_{\text{inel}}$  that should be used. This approach is certainly not working, but we keep it as an example to show what not to do.

*“Modified rescattering” approach* Finally, we implement an elaborate approach that is modified from the one studied in [14, 16, 23]. We first introduce a few concepts before going to the steps of implementation.

Comparing to previous works, we define an “effective” mean-free-path  $\tilde{\lambda}$ ,

$$\tilde{\lambda} = \frac{m_D^2}{\hat{q}_g(\omega, T)} \quad (13)$$

Unlike the mean-free-path that may be sensitive to the regulator, it only relates to well defined quantities and also applies to models with diffusion approximation of elastic processes so long as  $\hat{q}$  is given. We benefit from this feature and implement a general case where large-angle ( $|\hat{t}| > hm_D^2$ ) elastic scatterings are solved by a rate equation while small-angle ( $|\hat{t}| < hm_D^2$ ) processes are solved by a diffusion equation with  $\hat{q}_g(|\hat{t}| < hm_D^2)$ . Similarly, the inelastic processes are also separated into a large-angle triggered  $2 \rightarrow 3$  scattering (Equation 7 with  $|\hat{t}| > hm_D^2$ ) and a small-angle diffusion induced radiation part Equation 9 with  $\hat{q}_g(|\hat{t}| < hm_D^2)$ . Though this separation is shown to be equivalent to the leading order transport equation [24], it improves the model in the following ways. First, the model is not plagued by a rate that diverges when  $\hat{t} \rightarrow 0$ . Second, a tuning of  $h$  interpolates the model between the diffusion picture and the scattering picture. Third, one can employ parametric form instead of the leading order calculation of  $\hat{q}_g(|\hat{t}| < hm_D)$  to extract parameters from a model-to-data comparison.

Another change is the redefinition of the gluon formation time off a quark,

$$\tau_f = \frac{2(1-x)\omega}{(1-x + C_F/C_A x^2) k_{\perp}^2 + (1-x)m_g^2}. \quad (14)$$

The additional factor in front of  $k_{\perp}^2$  is motivated by the theory to be discussed in the next Section. It means that the system under consideration is not only a gluon but a system consists of both the mother quark and daughter partons. This factor goes back to one in the soft limit  $x \ll 1$ , but it increases the formation time for harder splitting.

With these building blocks, we present the following step-by-step implementation,

1. Within  $\Delta t$ , a mother parton undergoes both large-angle inelastic scattering and diffusion induced radiation with rates from Equations 7 and 9.
2. If a gluon  $i$  is sampled at  $t_{i,0}$ , it is appended to a “pre-gluons” list associated to the mother parton. But its energy is not carried away.
3. Loop over the “pre-gluons” list.

- 3.1 If  $\tau_f > t - t_{i,0}$ , evolve this gluon by both large-angle elastic scatterings and small-angle diffusion. Recalculate its formation time.
- 3.2 If  $\tau_f < t - t_{i,0}$ , accept it with probability  $p = \min\{1, u\tilde{\lambda}/\tau_f\}$ . Accepted gluons are formed and their energies are subtracted from the mother. Otherwise, they are removed from the list without causing energy loss.

4. Repeat for the next time step.

Here, we use the term “pre-gluons” to denote those gluons that stays in coherence with the mother parton. A parton may carry an arbitrary number of “pre-gluons” and there are no correlations among them. The formation time calculated after multiple scatterings scales like  $\sqrt{\omega/\hat{q}}$  on average, so the factor  $\tilde{\lambda}/\tau_f$  guarantees that the radiation spectra in the LPM region scales like the qualitative one in Equation 3. Now we explain the meaning of the other factor  $u$ . We first point out that the formation time from the above procedure is only valid to leading-log level. In the Monte-Carlo simulation, the final transverse momenta  $k_\perp^2 \sim \tau_f \hat{q} \sim \tau_f \alpha_s^2 T^3 \ln(Q_0^2/m_D^2)$ , and  $Q_0^2 \sim \hat{s}$  is the maximum momentum transfer squared in each elastic scattering. However, from a total coherent point of view, these re-scatterings act like a single one except that the maximum  $Q_0^2$  should be of the order of  $k_\perp^2 = \tau_f \hat{q}$ . Therefore, there is a mismatch in the argument of the logarithm. The  $u$  term is introduced to correct for this mismatch,

$$u = \left\{ \frac{\ln \left( 1 + \frac{\tau_f \hat{q}}{m_D^2} \right)}{\ln \left( 1 + \frac{\hat{s}}{m_D^2} \right)} \right\}^{\frac{1}{2}} \approx \left\{ \frac{\ln \left( 1 + \tau_f / \tilde{\lambda} \right)}{\ln \left( 1 + \frac{6\omega T}{m_D^2} \right)} \right\}^{\frac{1}{2}} \quad (15)$$

where we have used  $\langle \hat{s} \rangle \approx 6\omega T$ . This is also motivated by the next-to-leading-log approximation of AMY equation quoted in the next section.

Finally, we point out that Equations 13 and 14 only encodes the scaling of these quantities, so in practice we introduce the following tunable relations,

$$\begin{aligned} \tau_f &\rightarrow C_1 \tau_f, \\ \tilde{\lambda} &\rightarrow C_2 \tilde{\lambda}. \end{aligned} \quad (16)$$

The parameters  $C_1$  and  $C_2$  are ones by default and controls the finite- and infinite-size behaviors. This is possible by realizing that the comparison between medium length and the formation time solely determines the finite size effect; while the acceptance alone controls the magnitude of suppression. Though it is possible to fine-tuning these parameters systematically, we will show that the default  $C_1 = 1, C_2 = 1$  already works very well.

#### IV. SEMI-ANALYTIC FORMULA FOR RADIATIVE ENERGY LOSS

The full lead-order calculation in a “brick” medium and the comparison between different approximations

have been discussed in detail in [25]. The full calculation is complicated so we only quote its numerical calculation of radiation spectra in a finite medium. For other comparisons in a static medium, we make use of two (semi-)analytic results where medium induced gluon radiation is solved in an infinitely large medium (to next-to-leading-log accuracy) [26] and in a thin medium (to leading-log accuracy) [27]. We also use a valuable calculation performed for expanding medium [28], as it is much closer to the real collisions than a static one. For readers convenience, we briefly summarize the formula borrowed from [26–28] in this section.

In an infinite static medium, the formula for gluon radiation spectrum (we only use the one for gluon splitting from a quark) is derived in [29, 30],

$$\begin{aligned} \frac{dP_{q \rightarrow qg}}{dt dx} &= \frac{1}{2E\nu_q} \frac{\alpha_s d_F P_{q \rightarrow qg}(x)}{2x^2(1-x)^2} \int \frac{d^2\vec{h}}{(2\pi)^2} 2\vec{h} \cdot \Re e \vec{F} \\ &\times [1 + f_g(xp)][1 - f_q((1-x)p)], \end{aligned} \quad (17)$$

where  $\vec{F}(\vec{h}; p, x)$  satisfies the following equation,

$$\begin{aligned} 2\vec{h} &= i \frac{h^2 \vec{F}(\vec{h})}{p^3 2x(1-x)} \\ &+ g^2 \int \frac{dq_\perp^2 \mathcal{A}(q_\perp^2)}{(2\pi)^2} \left\{ \frac{C_A}{2} \left[ \vec{F}(\vec{h}) - \vec{F}(\vec{h} + p\vec{q}_\perp) \right] \right. \\ &+ \left( C_F - \frac{C_A}{2} \right) \left[ \vec{F}(\vec{h}) - \vec{F}(\vec{h} - xp\vec{q}_\perp) \right] \\ &\left. + \frac{C_A}{2} \left[ \vec{F}(\vec{h}) - \vec{F}(\vec{h} - (1-x)p\vec{q}_\perp) \right] \right\}. \end{aligned} \quad (18)$$

The collision kernel of a gluon in a thermalized QGP is,

$$\mathcal{A}(q_\perp^2) = \frac{T m_D^2}{q_\perp^2 (q_\perp^2 + m_D^2)}. \quad (19)$$

The exact solution can be obtained numerically, but the author of [26] obtained a semi-analytic solution to the next-to-leading-log ( $[\ln(E/T)]^{-1}$ ) accuracy that is easier to use,

$$\frac{dP_{q \rightarrow qg}^{\text{NLL}}}{dt dx} = \frac{\alpha_s P_{q \rightarrow qg}(x)}{2\pi} \frac{\sqrt{2} d_F}{\nu_q} \frac{m_D^2 \hat{\mu}_\perp^2(x)}{2x(1-x)E}. \quad (20)$$

Because we do not use quantum statistics in the Monte Carlo simulations, we have dropped the Bose enhancement and the Pauli blocking factors compared to the original formula. The remaining terms are organized so that the last factor plays the role of the inverse formation time. The dimensionless quantity  $\hat{\mu}_\perp^2(x)$  is determined by the self-consistent condition,

$$\begin{aligned} \hat{\mu}_\perp^2 &= \frac{gT}{m_D} \sqrt{\frac{2x(1-x)E}{\pi T}} \left\{ \frac{C_A}{2} (1-x)^2 \ln \left[ \frac{\xi \hat{\mu}_\perp^2}{(1-x)^2} \right] \right. \\ &\left. + \left( C_F - \frac{C_A}{2} \right) x^2 \ln \left( \frac{\xi \hat{\mu}_\perp^2}{x^2} \right) + \frac{C_A}{2} \ln(\xi \hat{\mu}_\perp^2) \right\}^{\frac{1}{2}}. \end{aligned} \quad (21)$$

$\xi \approx 9.09916$  is a constant. The NLL result is a good approximation when  $\ln(xE/T)$  is large. It shoots above

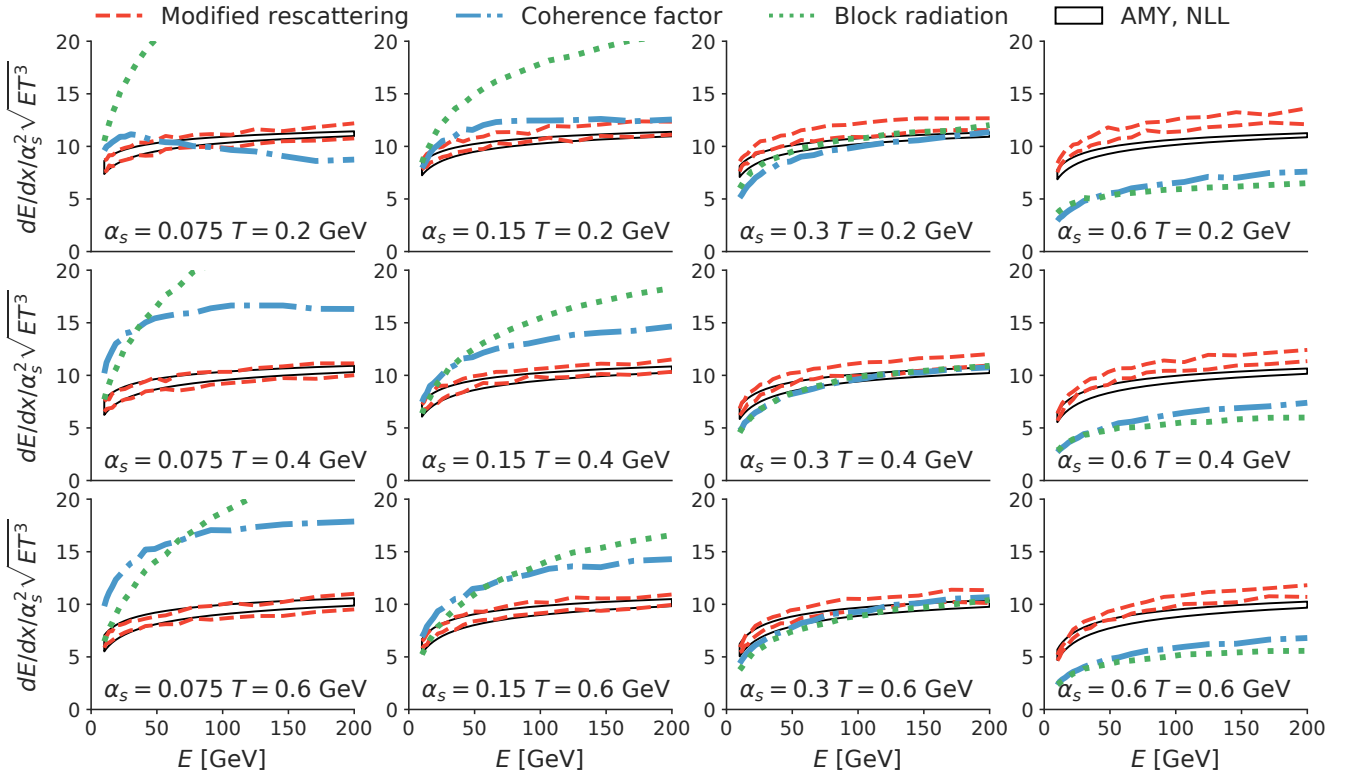


FIG. 1. Energy loss per unit path length  $dE/dx$  as a function of energy  $E$ , temperature  $T$  and coupling constant  $\alpha_s$ . Each column corresponds to  $\alpha_s = 0.075, 0.15, 0.3$ , and  $0.6$  (from left to right). Each row corresponds to  $T = 0.2, 0.4$ , and  $0.6$  GeV (from top to bottom).  $dE/dx$  is divided by the expected scaling  $\alpha_s^2 \sqrt{ET^3}$ . The calculations from “Modified rescattering”, “Coherence factor”, and “Block radiation” approaches are the red-dashed lines, blue-dash-dotted lines, and green-dotted lines respectively. The AMY NLL results are denoted as black boxes.

the numerical solutions with some universal behaviors when  $\ln(xE/T)$  is small. We compensate the difference by including an artificial multiplicative correction factor to Equation 20,

$$R_{\text{corr}} = \frac{1}{1 + 0.8 (xE/T)^{-0.7}}. \quad (22)$$

It mimics the systematic deviation of Equation 20 from the numerical solution. Later we will see that this is not a big effect for the relevant temperatures and parton energy larger than 10 GeV.

To see the physical interpretation of  $\hat{\mu}_\perp^2$ , we also quote the lead-log result from [26] (terms reorganized),

$$\begin{aligned} \frac{m_D^2 \hat{\mu}_{\perp,\text{LL}}^2}{2x(1-x)E} &= \left( \frac{4C_A \alpha_s T m_D^2 \ln(Q_0^2/m_D^2)}{2x(1-x)E} \right)^{\frac{1}{2}} \\ &\times \left( 1 - x + \frac{C_F}{C_A} x^2 \right)^{\frac{1}{2}} \end{aligned} \quad (23)$$

The logarithmic term comes from the integration of  $q_\perp^2 A(q_\perp^2) dq_\perp^2$  that yields  $\hat{q}$ .  $Q_0^2$  is an estimated upper limits of the integration. We see that the spectrum is

proportional to  $\sqrt{\hat{q}/\omega}$ , corroborating the previous qualitative arguments. The factor in the second line is included in the formation time redefinition in Equation 14 of the “modified rescattering” approach. At the NLL order,  $Q_0^2/m_D^2$  (equivalently  $\hat{\mu}_\perp^2$ ) is improved by the self-consistent Equation 21 that  $Q_0^2/m_D^2 \sim \sqrt{\hat{q}\omega}/m_D^2 \sim \tau_f \hat{q}/m_D^2$ . This is corrected in the “Modified rescattering” approach by the  $u$  factor in the acceptance.

For the case of a thin medium, a compact result is derived in [27]. It already combines the contributions from one single hard scattering and multiple soft scatterings. The energy loss reads,

$$\Delta E = \pi C_F C_A N_0 \alpha_s^3 T^3 L^2 \ln \left( \frac{E}{m_D^2 L} \right). \quad (24)$$

The factor  $N_0 = 6\zeta(3)(1+N_f/4)/\pi^2 \approx 1.28$  are obtained using quantum statistics for  $N_f = 3$ , but it is very close to the value calculated using classical statistics ( $12/\pi^2 \approx 1.22$ ,  $N_f = 3$ ). Therefore, we will not correct it in the comparison of the next Section.

In an expanding medium whose temperature follows a power law,

$$T^3 = T_0^3 \left( \frac{\tau_0}{\tau} \right)^{2-1/\nu} \quad (25)$$

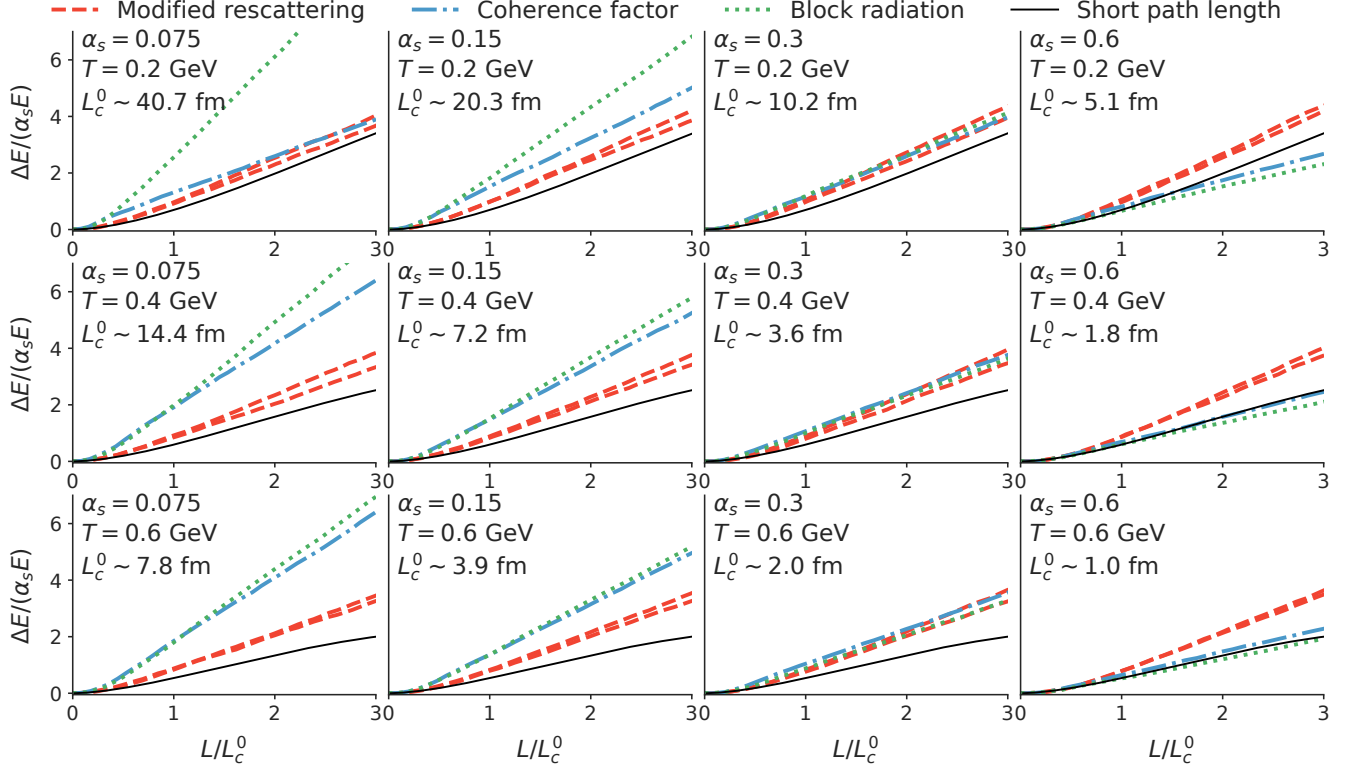


FIG. 2. Energy loss  $\Delta E$  as a function of path length  $L$ , temperature  $T$  and coupling constant  $\alpha_s$ . Each column corresponds to  $\alpha_s = 0.075, 0.15, 0.3$ , and  $0.6$  (from left to right). Each row corresponds to  $T = 0.2, 0.4$ , and  $0.6$  GeV (from top to bottom).  $\Delta E$  is scaled by  $\alpha_s E$  and  $L$  is scaled by an estimated critical path length  $L_c^0 = \sqrt{E/\hat{q}_0}$ ,  $\hat{q}_0 = C_A \alpha_s T m_D^2$ . The calculations from “Modified rescattering”, “Coherence factor”, and “Block radiation” approaches are the red-dashed lines, blue-dash-dotted lines, and green-dotted lines respectively. The analytic results for thin medium are denoted as black solid lines.

The authors of [28] found the radiation spectra as,

$$\frac{dP}{dx} = \frac{\alpha_s}{2\pi} P_{q \rightarrow qg}(x) \Re e \int_{\tau_0}^{\tau_0+L} \frac{dt_f}{t_f} \int_{\tau_0}^{t_f} \frac{dt_i}{t_i} \frac{1}{\nu^2} \quad (26)$$

$$[I_{\nu-1}(z_i)K_{\nu-1}(z_f) - I_{\nu-1}(z_f)K_{\nu-1}(z_i)]^{-2} \Big|_{\omega=\infty},$$

$$z_{i,f} = 2i\nu \sqrt{\frac{\hat{q}_g(1-x+C_F/C_A x^2)}{2(1-x)\omega}} \tau_0 \left( \frac{t_{i,f}}{\tau_0} \right)^{1/2\nu} \quad (27)$$

For  $\nu = 0.5$ , it reduces to the static BDMPS result [9]. The Bjorken expansion  $T \propto \tau^{-1/3}$  can be reached by taking the limit  $\nu \rightarrow 1$  [31]. In an expanding medium, e.g.  $\nu = 1$ , the transverse momentum broadening is,

$$\langle k_\perp^2 \rangle \sim \int_{t_1}^{t_1+\tau_f} \hat{q}(t) dt \sim \frac{t_1}{\tau_f} \ln \left( 1 + \frac{\tau_f}{t_1} \right) \hat{q}(t_1) \tau_f \quad (28)$$

So if the formation time is very short compared to the typical expansion time scale  $d \ln(T)/d\tau \sim t_1$ , the transverse broadening becomes  $\langle k_\perp^2 \rangle \sim \hat{q}(t_1) \tau_f$ , same as the one obtained in a static medium defined by the local temperature at  $t_1$ . But for large formation time,  $\langle k_\perp^2 \rangle$  becomes significantly smaller than the one determined using a local static medium. We will come back to the

impact of a local approximation in the next section. The BDMPS calculation takes the multiple-soft approximation, so we only use it in a thick enough medium such that,

$$\omega_c \sim \langle k_\perp^2 \rangle L > E. \quad (29)$$

A final remark is that all these analytic formulas are derived in the eikonal limit, so correspondingly in the Monte-Carlo simulations, we reset mother parton’s four momentum back to the initial one after each time step and the gluon four-momentum is rescaled such that the energy is unchanged.

## V. RESULTS

In this section, we compare the calculations of the three different implementations described in Section III to the theoretical limits quoted in Section IV. It is easier to compare the energy loss first, because it depends on an integration of the spectrum and not its details. It will be shown that the “Modified rescattering” approach has the best performance. We will also validate its radiation spectrum.

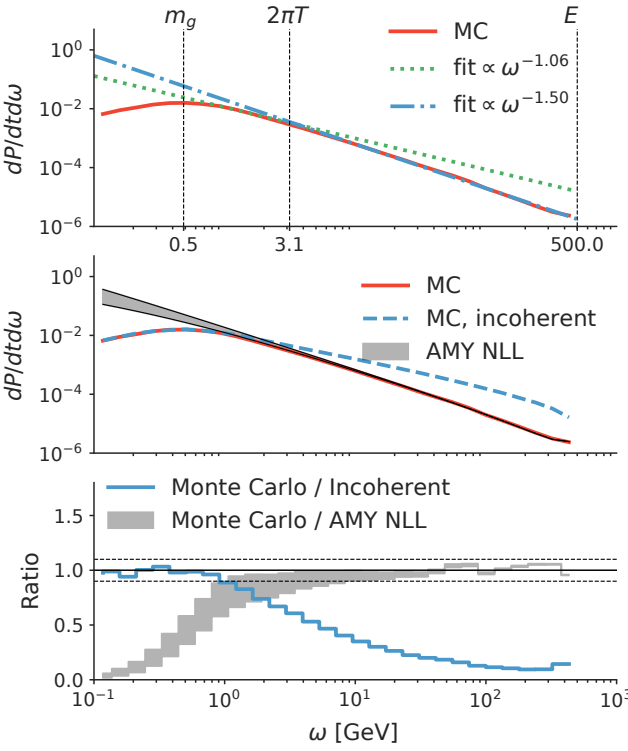


FIG. 3. Radiated gluon spectrum in an infinite medium from a quark  $E = 500$  GeV,  $\alpha_s = 0.1$ . The top plot shows the spectrum (red-dashed line) and power law fit (green-dotted and blue-dash-dotted lines) in different gluon energy ( $0 < \omega < E$ ) regions, separated by energy scale  $m_g$ ,  $\hat{q}_0 \lambda_g^2 \sim 2\pi T$ . The middle plot is the same simulation compared to the incoherent spectrum and the AMY semi-analytic result. The bottom plot is the ratio between the Monte-Carlo simulation and the semi-analytic calculation.

In Figure 1, we show the calculation of energy loss per unit path length  $dE/dx$  of a quark in an “infinitely large” medium. Technically,  $dE/dx$  is measured after a time evolution long enough ( $L \gg L_c$ ) that finite size effect has faded away. The results presented are further divided by the anticipated scaling  $dE/dx \propto \alpha_s^2 \sqrt{ET^3}$ . For each column, we double the  $\alpha_s$  value and for each row, temperature is increased by 0.2 GeV. Within each subplot, the parton energy varies from 10 GeV to 200 GeV. Different Monte Carlo calculations are shown in colored lines, AMY NLL results are shown as black boxes (we only integrate  $\omega$  above the Debye mass to calculate the AMY energy loss). The lower- and upper-bounds of the black boxes correspond to the results with or without the correction factor 22. We found that the “Modified rescattering” approach (red-dashed lines) well reproduces the energy, temperature, and coupling constant dependence of AMY NLL energy loss. The “Coherence factor” approach (blue-dash-dotted lines) has a similar energy and temperature dependence to those of the theoretical calculations; however, it systematically deviates from the

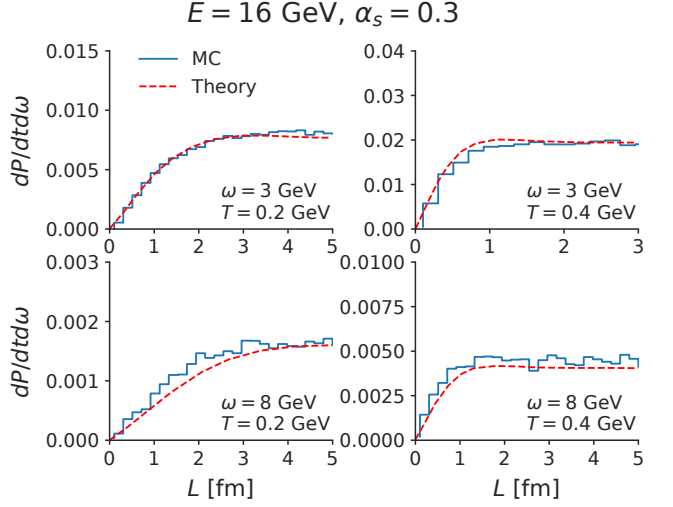


FIG. 4. Compare the path-length dependent energy-differential rate  $dP/(dtd\omega)$  from Monte-Carlo simulation using  $\alpha_s = 0.3$  to the theoretical calculation [25]. The light quark energy is 16 GeV. For each  $\omega$ , the gluon energy within  $\omega \pm 0.5$  GeV are used to compute the differential rate.

theory for different coupling constant in a logarithmic manner. For the “Block radiation” approaches, this  $\alpha_s$ -dependence deviation are even bigger and the energy dependence also gets worse, which are not surprised as we have discussed its problems in Section III.

Next we examine the path-length ( $L$ ) dependence of the energy loss  $\Delta E$  of a quark with  $E = 106$  GeV in a finite medium in Figure 2. Again, each column uses a different coupling constant and each row uses a different temperature. The path length within each subplot is varied up to four times of  $L_c^0$ . Here  $L_c^0 = \sqrt{E/\hat{q}_0}$  with  $\hat{q}_0 = C_A \alpha_s T m_D^2$  estimates the critical path length below which one expects a clear non-linear path-length dependence. All three implementations show the non-linear increase of  $\Delta E$  as function of  $L$ . The “Modified rescattering” approach stays close to the theory calculations when  $L < L_c^0$  for all cases, while the other two approaches deviates systematically as  $\alpha_s$  changes.

Finally, we validate the gluon radiation spectrum using the “Modified rescattering” approach. The spectrum in an infinite medium  $dP/dtd\omega$  is shown in Figure 3 for a 500 GeV quark. Please also refer to Appendix C for a full comparison varying both the quark energy and the coupling constant. The spectrum with  $\omega < m_g$  is suppressed due the use of a finite mass. In the Bethe-Heitler region  $m_g < \omega < 2\pi T$ , incoherent  $2 \rightarrow 3$  processes described in Equation 7 dominate and the spectrum scales like  $\omega^{-1}$ . In the LPM region  $2\pi T < \omega < E$ , the spectrum is dominated by coherent multiple scatterings and

FIG. 5. The top plot shows the radiation spectrum of BDMPS formula (symbols) and Monte-Carlo simulations (lines) in a static medium (blue points and lines with higher values) and a Bjorken expanding medium (red points and lines with lower values). In the bottom plot, we take ratios of the analytic results and simulations between the static and expanding medium cases. The parameters are  $\alpha_s = 0.3$ ,  $\tau_0 = 0.2 \text{ fm}/c$ ,  $\tau_0 + L = 20 \text{ fm}/c$ ,  $T_0 = 1 \text{ GeV}$ .

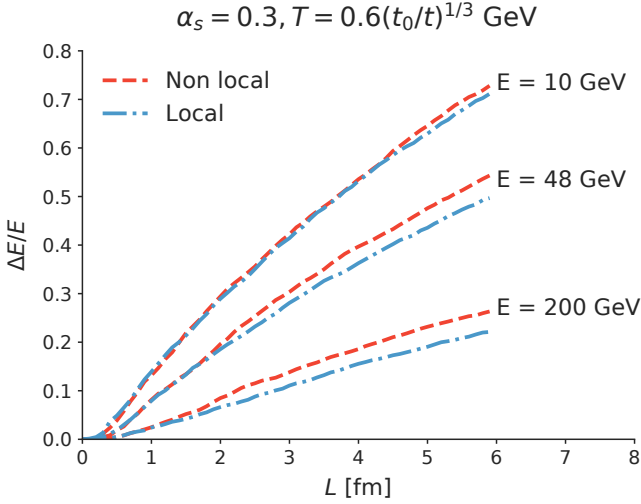


FIG. 6. Energy loss fraction  $\Delta E/E$  as function of path length  $L$  at three different energies. Red-dashed lines are direct simulations (the non-local case) and blue-dash-dotted lines are results using local approximation.

should be proportional to  $\omega^{-3/2}$ . The power-law fits in each domain are very close to the expected scaling. In the middle plot, we compare the above Monte-Carlo simulation to a simulation using incoherent rate and to the AMY NLL approximation. Their ratios are shown in the bottom plot. The “Modified rescattering” approach with  $C_1 = 1$  and  $C_2 = 1$  reproduces the incoherent limit with gluon thermal mass for  $\omega < 2\pi T$  and the LPM suppression for  $\omega > 2\pi T$  within about 20% accuracy. In Figure 4, the spectrum in a finite medium is compared to the full calculations from [25]. Using  $\alpha_s = 0.3$ , we calculated the  $L$ -dependent gluon radiation rate of a 16 GeV quark. Medium temperature of the left and the right columns are 0.2 GeV and 0.4 GeV respectively. Top and bottom rows show the differential rates for emitting gluon with  $\omega = 3 \text{ GeV}$  and  $\omega = 8 \text{ GeV}$ . In practice, we counted events within a finite range  $\omega \pm 0.5 \text{ GeV}$ . The radiation spectrum is recovered to a similar level of accuracy as the infinite medium case.

Next, the comparison to the BDMPS calculation in expanding medium is shown in Figure 5. We only turn on the diffusion and the diffusion induced radiation processes in “Modified rescattering” approach, because it allows using the same  $\hat{q}_g$  in both the BDMPS formula and the Monte-Carlo simulation. Here, we simply choose

$\hat{q}_g = m_D^2 C_A \alpha_s T$ . The top plot of Figure 5 compares the spectra to theory in both static and expanding cases. The expansion starts from  $\tau_0 = 0.2 \text{ fm}/c$  with  $T_0 = 1 \text{ GeV}$ . The evolution stops at  $\tau = 20 \text{ fm}/c$  with  $T \approx 0.22 \text{ GeV}$ . One can check that for a 100 GeV quark and  $\alpha_s = 0.3$ , the requirement of Equation 29 is satisfied. The static medium lasts the same amount of time with its temperature stays at  $T_0$ . The spectrum in the expanding medium is well described by the simulation, meaning that the “Modified rescattering” approach can be applied to parton evolution in a dynamical medium. The bottom plot shows the ratio between the two cases. The expansion reduces the spectra by almost a factor of 10 compared to the static case.

We have briefly mentioned the local approximation in the discussion following Equation 28. When the medium expansion rate is large compared to the inverse formation time, the following two scenarios are different,

1. *A non-local (direct) calculation:* radiated gluons can precept the changing medium within the formation times.
2. *A local approximation:* calculate with rates obtained in the infinite medium defined by the local temperature at the radiation vertex.

Here we study how good the local approximation is for a typical coupling  $\alpha_s = 0.3$ . The “Modified rescattering” approach is already a non-local calculation, because it performs gluon rescatterings at different space-time during the evolution. To mimic the local approximation, we let each pre-gluon  $i$  remember the temperature  $T_i$  when it is first created and then perform rescatterings in an “imaginary medium” defined by  $T_i$ . The results are shown in Figure 6. The difference between the two scenarios are negligible for  $E = 10 \text{ GeV}$  and is only moderate for a 200 GeV quark. This is because for  $\alpha_s = 0.3$ , the ratio of the estimated maximum formation time  $\sqrt{2x(1-x)E/\hat{q}_0}$  to the inverse temperature changing rate  $(d\ln(T)/dt)^{-1}$ ,

$$L_c \frac{d\ln(T)}{dt} = \sqrt{\frac{0.5E}{6\pi C_A \alpha_s^2 T_0^3 9\tau_0}} \approx \sqrt{\frac{0.7 \text{ fm}/c}{\tau_0 + L}} \quad (30)$$

is not large after a few fermis. In more realistic event-by-event hydrodynamics simulations, the temperature profiles are much more complicated. Initial condition fluctuations create medium hot spots and radial expansion boosts the fluid local rest frame. So it is still premature to conclude from this study in Bjorken flow that the local approximation is also justified in event-by-event simulations.

## VI. THE INCLUSION OF RUNNING COUPLING AND MASS EFFECT

This section focus on improving the model with running coupling and mass effects. However, due to their

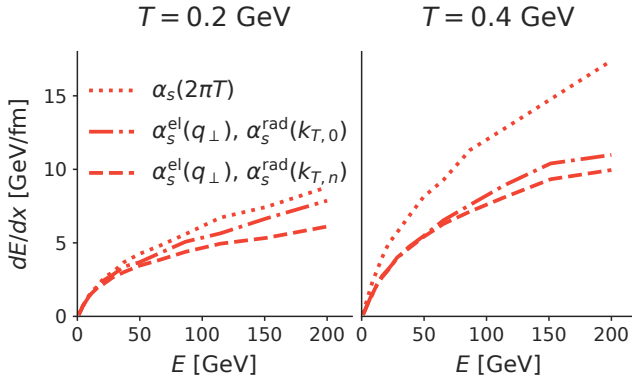


FIG. 7. Impact of the running coupling constant on the radiative energy loss. The dotted lines are calculated using fixed coupling  $\alpha_s(2\pi T)$  for reference. The dash-dotted lines uses the prescription  $\alpha_s^{\text{el}}(q_\perp)$  and  $\alpha_s^{\text{rad}}(k_{\perp,0})$ . The dashed lines further modify the radiation vertex with  $\alpha_s^{\text{rad}}(k_{\perp,n})$ .

complexity, we did not find applicable theory results to compare to. As a result, the proposed methods in this section should be considered as tentative.

First we replace the fixed coupling by a running one following the prescription described in [26]. This involves two changes in the formula. For elastic scattering vertices,  $\alpha_s^{\text{el}}$  is evaluated at the  $t$ -channel momentum transfer squared. This is already the feature of Lido. For splitting vertices,  $\alpha_s^{\text{rad}}$  should be evaluated at the final gluon transverse momenta squared,

$$k_{\perp,n}^2 = \left( \vec{k}_{\perp,0} + \vec{q}_1 + \cdots + \vec{q}_n \right)^2. \quad (31)$$

In the Lido model, the original scale used for  $\alpha_s^{\text{rad}}$  is  $k_{\perp,0}^2$  from the  $2 \rightarrow 3$  process. Therefore, we modify the acceptance probability  $p$  to

$$p' = \min \left\{ 1, u \frac{\tilde{\lambda}}{\tau_f} \frac{\alpha_s(k_{\perp,n})}{\alpha_s(k_{\perp,0})} \right\}. \quad (32)$$

The order of magnitude of  $k_{\perp,n}^2$  is  $\sqrt{\hat{q}\omega}$  and it is about  $\sqrt{\omega/T}$  times larger than  $k_{\perp,0}^2$  for gluons in the LPM region, therefore the running coupling effect suppress the spectrum by another factor of  $\alpha_s(k_{\perp,n})/\alpha_s(k_{\perp,0})$ . In Figure 7, we showed three calculations in a static medium. The dotted lines, as references, use a fixed coupling constant evaluated at a thermal scale  $\alpha_s = \alpha_s(2\pi T)$ . This scale is also the lowest scale cut-off for the running coupling constant in our model (note that this minimum scale is not required in the original work [26]). The dash-dotted lines are running coupling calculations where the  $\alpha_s^{\text{el}}$  is evaluated at  $\hat{t}$  and the  $\alpha_s^{\text{rad}}$  at  $k_{T,0}$ . The dashed lines are also running coupling calculations but evaluate  $\alpha_s^{\text{rad}}$  at  $k_{\perp,n}$  through the modified acceptance  $p'$ . The running coupling effect results in a reduction of the energy loss compared to the fixed coupling references.

Second, we put back the mass effects to treat the heavy quarks. These include the massive particle kinematics, a

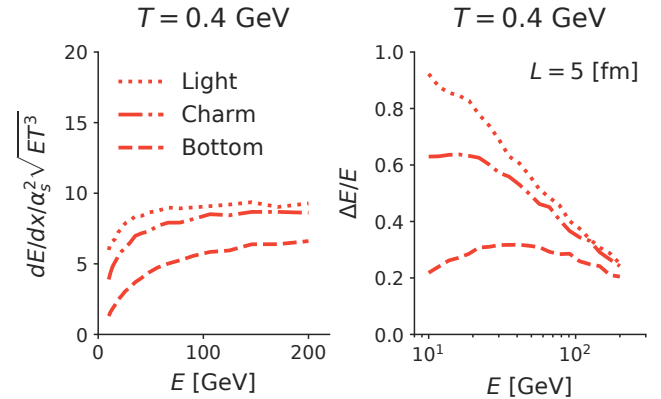


FIG. 8. A demonstration of mass effect with  $\alpha_s = 0.3$ . Left plot: the scaled energy loss rate in an infinite medium for light quark, charm quark and bottom quark. Right plot: energy loss fraction of light quark, charm quark and bottom quark at path length  $L = 4$  fm.

substitution in the formation time,

$$(1-x)m_g^2 \rightarrow x^2 M^2 + (1-x)m_g^2 \quad (33)$$

and the so-called “dead-cone” effect that suppresses collinear radiations with angles  $\theta \sim k_\perp/k < M/E$ . The massive version of the  $2 \rightarrow 3$  improved Gunion-Bertsch matrix-element has been derived in [20]. If we simply replace the matrix-element with the massive one, the dead cone suppression involves the factor,

$$\frac{k_{\perp,0}^2}{k_{\perp,0}^2 + x^2 M^2} \quad (34)$$

However, because rescatterings continue to increase the average  $k_\perp^2$ , the factor is different by the time the gluon is formed,

$$\frac{k_{\perp,n}^2}{k_{\perp,n}^2 + x^2 M^2}. \quad (35)$$

The solution is to use the  $2 \rightarrow 3$  matrix-element without mass effect to generate pre-gluons, while implementing the dead-cone suppression by adding another factor to the acceptance,

$$p'' = \min \left\{ 1, u \frac{\tilde{\lambda}}{\tau'_f} \frac{\alpha_s(k_{\perp,n})}{\alpha_s(k_{\perp,0})} \left[ \frac{k_{\perp,n}^2}{k_{\perp,n}^2 + x^2 M^2} \right]^4 \right\}. \quad (36)$$

On the left of Figure 8, the scaled energy loss rate in an infinite medium is extracted from simulations for light (massless), charm ( $M = 1.3$  GeV) and bottom ( $M = 4.2$  GeV) quarks. On the right, it is the energy loss fraction at a fixed path-length  $L = 5$  fm. In both cases, the mass introduces the energy loss ordering,  $\Delta E_{\text{light}} > \Delta E_c > \Delta E_b$  and the differences decrease at higher energy.

## VII. SUMMARY AND OUTLOOK

To reduce the theory uncertainty introduced in the numerical implementation of the perturbative QCD transport of hard partons inside a quark-gluon plasma, we studied three different Monte-Carlo implementations and compare them to theory calculations. We showed that the “Modified rescattering” approach reproduces the coupling constant, temperature, parton energy and path-length dependences of the theoretical formula in both infinite- and thin-medium limits. This overall level of agreement between the simulated radiation spectrum to theory is promising given the simplicity and limits of a Monte-Carlo procedure. Tentative running coupling and dead-cone effect are also implemented. For future studies, controlling the uncertainties between Monte-Carlo implementation and theory helps to perform a more unambiguous examination of theory assumptions and a more meaningful phenomenology extraction of jet, heavy quark transport properties in a model-to-data comparison. Moreover, a Monte-Carlo generator that is tuned to match leading order theory calculation could be a good starting point to implement next-to-leading-order effects in the phenomenology model.

## ACKNOWLEDGMENTS

SAB, WK and YX are supported by the U.S. Department of Energy Grant no. DE-FG02-05ER41367. WK is also supported by NSF grant OAC-1550225.

### A. THE RUNNING COUPLING CONSTANT

The leading order running couplings constant with three flavors of quarks is

$$\alpha_s(Q) = \frac{4\pi}{9 \log(Q^2/\Lambda_{\text{QCD}}^2)}, \quad (37)$$

and  $\Lambda_{\text{QCD}} = 0.2$  GeV. In a medium, we require the scale of a process cannot be arbitrary smaller than the temperature. The resulting  $Q$  is cut off at a medium scale defined by  $\mu\pi T$  ( $\mu = 2$  by default) and  $\alpha_s(Q) = \alpha_s(\max\{Q, T\})$ . We treat  $\mu$  as a parameter of the model. It is also a major source of uncertainty in the predictions. In fact for a typical  $T = 0.3$  GeV,  $\alpha_s(\pi T \sim 4\pi T)$  varies from 0.45 to 0.24.

### B. THE GUNION-BERTSCH RATE UNDER SOFT TRANSVERSE MOMENTA EXCHANGE.

The Gunion-Bertsch matrix-element factorizes the  $2 \rightarrow 3$  process into the product of a  $2 \rightarrow 2$  process and the

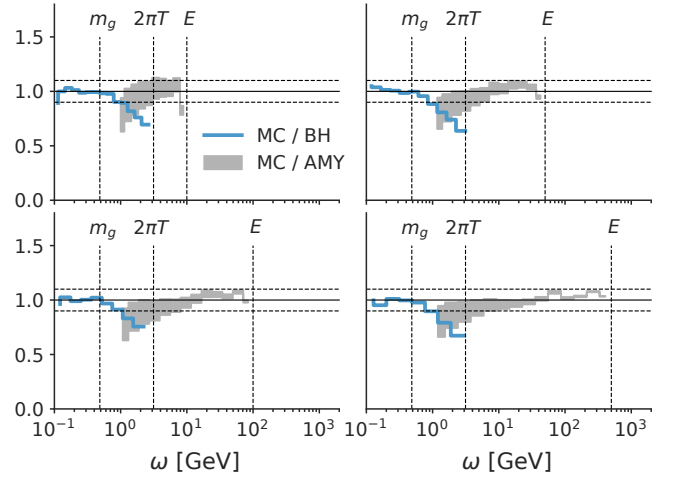


FIG. 9. The ratios of Monte-Carlo simulated spectra to the AMY NLL spectra (gray bands) and to the Gunion-Bertsch incoherent spectra (blue lines) are plotted, using  $\alpha_s = 0.1$ . The quark energy  $E$  is 10, 50, 100, and 500 GeV as indicated by the rightmost vertical dashed lines in each subplot. The horizontal dashed lines denote  $\pm 20\%$  deviation from unity.

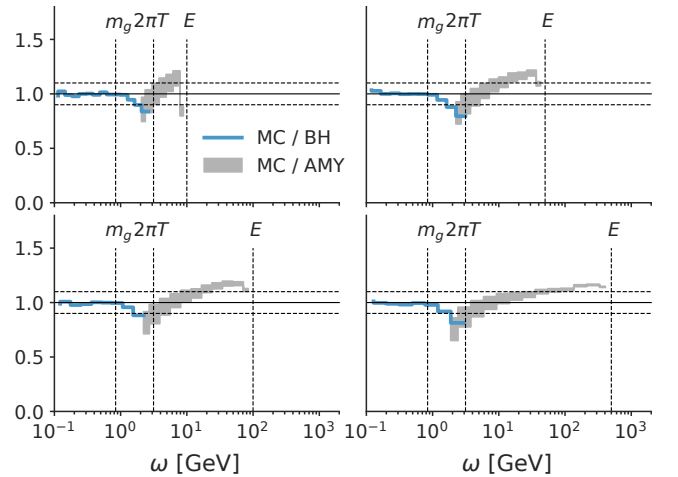


FIG. 10. The same as Figure 9, but for  $\alpha_s = 0.3$ .

radiative  $1 \rightarrow 2$  process. In the vacuum, this is,

$$|M_{\text{GB}}|^2 = |M_{2 \rightarrow 2}|^2 16C_A \pi \alpha_s \frac{(1 - \bar{x})^2 q_\perp^2}{k_\perp^2 (\vec{q}_\perp - \vec{k}_\perp)^2}. \quad (38)$$

In medium, a gluon thermal mass regulates the divergence. For hard splitting where  $k_\perp \gg q_\perp \sim m_D$ ,

$$|M_{\text{GB}}|^2 \approx q_\perp^2 |M_{2 \rightarrow 2}|^2 16C_A \pi \alpha_s \frac{(1 - \bar{x})^2}{k_\perp^4}. \quad (39)$$

Plug in this approximation in the scattering rate Equation 7 and factorize the  $q_\perp$  and  $k_\perp$  integrations,

$$\Gamma = \frac{1}{2E_1} \int \frac{f_i(p_2) d\vec{p}_2^3}{(2\pi)^3 2p_2} 2\hat{s} \int d\hat{t} \frac{d\sigma_{2 \rightarrow 2}}{d\hat{t}} q_\perp^2 \times \int 16\pi C_A \alpha_s \frac{(1-\bar{x})^2}{k_\perp^4} \frac{dk^3}{(2\pi)^3 2k} \quad (40)$$

For the case of a quark, the first integration over the  $2 \rightarrow 2$  cross-section gives  $C_F/C_A \hat{q}_g$ , after summing over degeneracy of the gluonic and the fermionic scattering centers. Then rewriting the second  $k$  integration in terms of  $x, k_\perp^2$  in the limit  $\bar{x} \ll 1$ , the rate becomes,

$$\Gamma = \hat{q}_g \int \frac{2C_F \alpha_s}{2\pi} \frac{dk_\perp^2}{k_\perp^4} \frac{dx}{x} \quad (41)$$

Finally, inserting the coherence factor of Equation 8, the gluon radiation rate becomes identical to the one used in [11] when  $x \ll 1$ . Reorganize the incoherent rate Equation 41 perform the  $k_\perp$  integration with the regulator  $m_g$ , we get,

$$\Gamma = \int \frac{\alpha_s}{2\pi} \frac{2C_F}{x} dx \frac{q_g}{m_g^2} \quad (42)$$

The factor  $\frac{q_g}{m_g^2}$  motivates our definition of the effective mean-free-path in Equation 13.

To estimate the order-of-magnitude of  $\Delta t$  in the coherence factor, apply the condition 10 and the above ap-

proximated formula,

$$\begin{aligned} 1 &\sim \alpha_s \hat{q} \Delta t \int \frac{d\omega}{\omega} \frac{dk_\perp^2}{k_\perp^4} \left[ 1 - \frac{\sin(\Delta t k_\perp^2 / 2\omega)}{\Delta t k_\perp^2 / 2\omega} \right] \\ &= \alpha_s \hat{q} \Delta t^2 \int \frac{d\omega}{2\omega^2} \int d \frac{2\omega}{\Delta t k_\perp^2} \left[ 1 - \frac{\sin(\Delta t k_\perp^2 / 2\omega)}{\Delta t k_\perp^2 / 2\omega} \right] \\ &= \alpha_s \hat{q} \Delta t^3 \int \frac{d(\omega \Delta t)}{2(\omega \Delta t)^2} f(2\omega \Delta t) \end{aligned} \quad (43)$$

The limiting behavior of function  $f(x)$  can be captured by a simple interpolation  $Ax/(B+x)$ , therefore the final integration only results in logarithmic dependence on the  $\omega_{\min} \Delta t$  and  $E \Delta t$ . So, the order of magnitude of a typical  $\Delta t$  is  $(\alpha_s \hat{q})^{-1/3} \sim 1/\alpha_s T$ .

### C. ENERGY AND COUPLING CONSTANT DEPENDENCE OF RADIATION SPECTRA

It is important that we are aware of the known discrepancies between the Monte-Carlo implementation and the theory, particularly if one investigates an observable that is sensitive to the details of the spectra. In this appendix, we provide comparisons of radiation spectra at different energy and coupling constants for readers references. Figure 9 and Figure 10 shows calculation using  $\alpha_s = 0.1$  and  $0.3$ . Within in each figure, different subplots vary the quark energy. The gray bands are the ratios between the simulations and the AMY-NLL results (plotted for  $\pi T < \omega < E$ ) and the blue lines are the ratios between the full simulations and the incoherent simulations (the Gunion-Bertsch rate, plotted for  $0.1 \text{ GeV} < \omega < 4\pi T$ ). We notice that there are residue systematic logarithmic discrepancies from low energy to high energy. The implementation also tends to generate less branching when  $x \rightarrow 1$ .

- 
- [1] A. Collaboration (ATLAS), (2012), [ATL-PHYS-PUB-2012-002](#), [ATL-COM-PHYS-2012-1116](#).
- [2] B. Abelev *et al.* (ALICE), *J. Phys.* **G41**, 087002 (2014).
- [3] Y. Wang and the Star Collaboration, *Journal of Physics: Conference Series* **535**, 012022 (2014).
- [4] A. Adare *et al.* (PHENIX), (2015), [arXiv:1501.06197](#) [nucl-ex].
- [5] C. Collaboration (CMS), (2017), [CMS-PAS-FTR-17-002](#).
- [6] A. B. Migdal, *Phys. Rev.* **103**, 1811 (1956).
- [7] X.-N. Wang, M. Gyulassy, and M. Plumer, *Phys. Rev.* **D51**, 3436 (1995), [arXiv:hep-ph/9408344](#) [hep-ph].
- [8] B. G. Zakharov, *JETP Lett.* **63**, 952 (1996), [arXiv:hep-ph/9607440](#) [hep-ph].
- [9] R. Baier, Y. L. Dokshitzer, A. H. Mueller, S. Peigne, and D. Schiff, *Nucl. Phys.* **B483**, 291 (1997), [arXiv:hep-ph/9607355](#) [hep-ph].
- [10] M. Djordjevic and U. W. Heinz, *Phys. Rev. Lett.* **101**, 022302 (2008), [arXiv:0802.1230](#) [nucl-th].
- [11] S. Cao, G.-Y. Qin, and S. A. Bass, *Phys. Rev.* **C88**, 044907 (2013), [arXiv:1308.0617](#) [nucl-th].
- [12] C. E. Coleman-Smith and B. Muller, *Phys. Rev.* **C86**, 054901 (2012), [arXiv:1205.6781](#) [hep-ph].
- [13] Z. Xu and C. Greiner, *Phys. Rev.* **C71**, 064901 (2005), [arXiv:hep-ph/0406278](#) [hep-ph].
- [14] K. C. Zapp, J. Stachel, and U. A. Wiedemann, *JHEP* **07**, 118 (2011), [arXiv:1103.6252](#) [hep-ph].
- [15] P. B. Gossiaux, *Proceedings, 5th International Conference on Hard and Electromagnetic Probes of High-Energy Nuclear Collisions (Hard Probes 2012): Cagliari, Italy, May 27-June 1, 2012*, *Nucl. Phys.* **A910-911**, 301 (2013), [arXiv:1209.0844](#) [hep-ph].
- [16] C. Park, *Jet energy loss with finite-size effects and running coupling in MARTINI*, Master's thesis, McGill University, Montréal, Québec (2015).
- [17] P. Arnold, H.-C. Chang, and S. Iqbal, *JHEP* **10**, 124 (2016), [arXiv:1608.05718](#) [hep-ph].

- [18] W. Ke, Y. Xu, and S. A. Bass, (2018), arXiv:1806.08848 [nucl-th].
- [19] O. Fochler, J. Uphoff, Z. Xu, and C. Greiner, Phys. Rev. **D88**, 014018 (2013), arXiv:1302.5250 [hep-ph].
- [20] J. Uphoff, O. Fochler, Z. Xu, and C. Greiner, J. Phys. **G42**, 115106 (2015), arXiv:1408.2964 [hep-ph].
- [21] S. Cao, T. Luo, G.-Y. Qin, and X.-N. Wang, Phys. Rev. **C94**, 014909 (2016), arXiv:1605.06447 [nucl-th].
- [22] S. Cao, T. Luo, G.-Y. Qin, and X.-N. Wang, Phys. Lett. **B777**, 255 (2018), arXiv:1703.00822 [nucl-th].
- [23] C. Park, C. Shen, S. Jeon, and C. Gale, *Proceedings, 8th International Conference on Hard and Electromagnetic Probes of High-energy Nuclear Collisions: Hard Probes 2016 (HP2016): Wuhan, Hubei, China, September 23-27, 2016*, Nucl. Part. Phys. Proc. **289-290**, 289 (2017), arXiv:1612.06754 [nucl-th].
- [24] J. Ghiglieri, G. D. Moore, and D. Teaney, JHEP **03**, 095 (2016), arXiv:1509.07773 [hep-ph].
- [25] S. Caron-Huot and G. D. Moore, JHEP **02**, 081 (2008), arXiv:0801.2173 [hep-ph].
- [26] P. B. Arnold and C. Dogan, Phys. Rev. **D78**, 065008 (2008), arXiv:0804.3359 [hep-ph].
- [27] P. B. Arnold, Phys. Rev. **D80**, 025004 (2009), arXiv:0903.1081 [nucl-th].
- [28] R. Baier, Y. L. Dokshitzer, A. H. Mueller, and D. Schiff, Phys. Rev. **C58**, 1706 (1998), arXiv:hep-ph/9803473 [hep-ph].
- [29] P. B. Arnold, G. D. Moore, and L. G. Yaffe, JHEP **01**, 030 (2003), arXiv:hep-ph/0209353 [hep-ph].
- [30] P. B. Arnold, G. D. Moore, and L. G. Yaffe, JHEP **05**, 051 (2003), arXiv:hep-ph/0302165 [hep-ph].
- [31] J. D. Bjorken, Phys. Rev. D **27**, 140 (1983).